AAS 24-161

GENERATING THE TRAJECTORY DESIGN SPACE FOR NEPTUNIAN SYSTEM EXPLORATION

Giuliana E. Miceli[*], Natasha Bosanac[†], Reza Karimi[‡]

This paper uses a motion primitive approach to explore a constrained trajectory tradespace for a spacecraft in the Neptunian system. First, motion primitives are generated to supply a subset of building blocks for more complex trajectories. A graph is then constructed to represent the potential for these primitives to be connected while satisfying path and maneuver constraints. Searching this graph produces an array of geometrically distinct initial guesses. After corrections and optimization, the result is a tradespace of constrained transfers from a high-energy interplanetary arrival condition to various scientific orbits.

INTRODUCTION

The only two planets within our solar system that have not been visited for substantial periods of time are Uranus and Neptune.[1] Often labeled as 'ice giants', these two planets are predominantly composed of ice-forming elements, e.g., oxygen and carbon; are significantly more massive than terrestrial planets; and possess many moons.[2] However, there are still many unknowns about the nature of the ice giants such as their formation, bulk and atmospheric composition, and presence of water oceans on their moons. These outstanding questions can likely only be answered through a dedicated planetary exploration mission.

The science and space exploration communities have formulated mission concepts for spacecraft to visit Neptune and Uranus for flybys, orbiters, and probes.[3–9] One important task for developing these concepts and missions is designing trajectories for a spacecraft that is operating within an ice giant system to support scientific observations. However, this task is challenging due to the often high-energy interplanetary arrival conditions; the complex solution space in a multi-body gravitational system at these high energies; the constraints imposed by spacecraft hardware, e.g., limited maneuvering capability; and mission and operational constraints. In this paper, we focus specifically on the trajectory design problem for a spacecraft operating in the Neptunian system.

To address the challenges of trajectory design within multi-body gravitational systems, Smith and Bosanac have developed a motion primitive approach;[10,11] and Miceli et al. have recently built upon this procedure.[12] This approach leverages the concept of motion primitives, used in the field of robotics, to represent the building blocks of motion. Then, complex trajectories are rapidly formed from sequences of motion primitives. When applied to the trajectory design problem by Smith and Bosanac, a motion primitive library is generated by using clustering to summarize arcs along selected periodic orbit families and their associated hyperbolic invariant manifolds in a low-fidelity model such as the circular restricted three-body problem (CR3BP).[10,11] A motion primitive graph is then formed to reflect their potential for connectivity. This motion primitive graph is searched to rapidly identify distinct primitive sequences that supply initial guesses for geometrically distinct transfers. These initial guesses are corrected using collocation and multi-objective optimization to generate continuous, maneuver-enabled paths in the CR3BP. Miceli et al. demonstrated that this approach can

[*]Graduate Research Assistant, Colorado Center for Astrodynamics Research, Smead Department of Aerospace Engineering Sciences, University of Colorado Boulder, Boulder, CO, 80303.

[†]Assistant Professor, Colorado Center for Astrodynamics Research, Smead Department of Aerospace Engineering Sciences, University of Colorado Boulder, Boulder, CO, 80303.

[‡]Outer Planet Mission Design Analyst, Mission Design and Navigation, Jet Propulsion Laboratory, California Institute of Technology, Pasadena, CA, 91109.

be used to design geometrically distinct spacecraft trajectories from a high-energy interplanetary arrival condition to a 3:4 resonant science orbit in the CR3BP.[12] These transfers can then be corrected in a higher-fidelity ephemeris model.

This paper builds upon our prior work by using a motion primitive approach to 1) generate constrained spacecraft trajectories within the Neptunian system and 2) explore a region of the trajectory trade space for various science-driven target orbits and spacecraft characteristics. We have updated the existing motion primitive trajectory design approach to incorporate path and hardware constraints. This information influences a spacecraft's operability and maneuverability and, as a result, can influence the characteristics of viable trajectories. Constraints considered in this paper are applied to the periapsis or apoapsis distance relative to primary bodies and maneuver magnitudes. Some of these constraints influence the inclusion and connectivity of motion primitives within the graph. For example, a primitive summarizing arcs that violate a path constraint is omitted from the graph. Alternatively, two primitives that are expected to require too large an impulsive maneuver between them would not be connected. In addition, these constraints are incorporated into the trajectory corrections and optimization procedure to ensure they are satisfied by the final solution.

The constrained motion primitive graph is then used to generate a region of the trajectory trade space. First, two target orbits and two arrival conditions are considered, capturing some of the trades that may be performed during the mission design process. Once motion primitive graphs have been constructed, initial guesses for transfers are generated using an updated k-shortest path algorithm to identify the most efficient, geometrically distinct sequences that are likely to satisfy the constraints. The resulting primitive sequences are then corrected and optimized in an ephemeris model along with the constraints and propulsion system characteristics.

BACKGROUND

Circular Restricted Three-Body Problem

The dynamics of a spacecraft in the Neptunian system are modeled using the Neptune-Triton Circular Restricted Three-Body Problem (NT-CR3BP), where the primary bodies are Neptune and Triton, labeled P_1 and P_2, and the third body is the spacecraft. This model assumes that the spacecraft possesses a negligibly small mass compared with the primaries, which is reasonable for the Neptune-Triton system. Moreover, P_1 and P_2 are modeled to have the same gravity field as a point mass with constant mass while following circular orbits about their barycenter.[13] Because Triton's orbit relative to Neptune has an eccentricity of 0.000016,[14] this assumption is also reasonable.

The formulation of the CR3BP involves defining both a rotating frame and a nondimensionalization scheme. In the rotating frame, the origin is located at the system barycenter whereas the axes $\hat{\boldsymbol{x}}, \hat{\boldsymbol{y}}, \hat{\boldsymbol{z}}$ are defined as follows: $\hat{\boldsymbol{x}}$ is directed from P_1 to P_2, $\hat{\boldsymbol{z}}$ is in the direction of the orbital angular momentum vector of the primary bodies, and $\hat{\boldsymbol{y}}$ completes the right-handed triad.[13] Finally, length, time and mass quantities are nondimensionalized by the characteristic quantities l^*, m^*, and t^*:[13] $m^* \approx 1.024569 \times 10^{26}$ kg is the sum of the masses of the primaries, $l^* = 354,760$ km is set equal to the average distance between the primaries, and $t^* \approx 8.081353 \times 10^4$ s sets the mean motion of the primary system to unity.[15]

In the CR3BP, the nondimensional equations of motion are expressed in the P_1 - P_2 rotating frame. First, the state of the spacecraft is defined as $\boldsymbol{x} = [x, y, z, \dot{x}, \dot{y}, \dot{z}]^T$, assuming an observer in the rotating frame. The equations of motion are then written in the rotating frame as

$$\ddot{x} = 2\dot{y} + \frac{\partial U^*}{\partial x}, \quad \ddot{y} = -2\dot{x} + \frac{\partial U^*}{\partial y}, \quad \ddot{z} = \frac{\partial U^*}{\partial z} \tag{1}$$

where

$$U^* = \frac{1}{2}(x^2 + y^2) + \frac{(1-\mu)}{r_1} + \frac{\mu}{r_2} \tag{2}$$

$$r_1 = \sqrt{(x+\mu)^2 + y^2 + z^2} \quad \text{and} \quad r_2 = \sqrt{(x-1+\mu)^2 + y^2 + z^2} \tag{3}$$

In these expressions, the mass ratio of the Neptune-Triton system is $\mu = M_2/(M_1 + M_2) \approx 0.00020895$. This model possesses only one integral of motion, the Jacobi constant, which is computed as $C_J = 2U^* - \dot{x}^2 - \dot{y}^2 - \dot{z}^2$.[13]

The solution space in the CR3BP includes fundamental solutions such as equilibrium points that are labeled L_i for $i = [1, 5]$, families of periodic and quasi-periodic orbits, and their hyperbolic invariant manifolds. Families of periodic orbits include paths that are periodic in the rotating frame after a minimal time labeled the period.[13] This paper uses periodic orbits that emanate from the collinear equilibrium points and their hyperbolic invariant manifolds, as well as resonant orbits. Consistent with their definition in the Keplerian dynamics, a spacecraft following a $p : q$ resonant orbit completes p revolutions around the larger primary body in approximately the time that the smaller primary body completes q revolutions in the inertial frame.[16] A resonant orbit is labeled as interior if $p > q$, and exterior when $q > p$; these resonant orbits can be either prograde or retrograde in the rotating frame. Hyperbolic invariant manifolds emanate from an unstable periodic orbit. Stable (or unstable) manifolds capture flow that asymptotically approaches the periodic orbit in forward (or backward) time.

Ephemeris Model

A point mass ephemeris model is also used to construct a high-fidelity model of the gravitational influence of Neptune and its main 14 moons. The equations of motion are formulated in an inertial frame; in this paper, using the axes of the International Celestial Reference Frame and the origin located at the center of Neptune. The state vector for the spacecraft relative to Neptune is defined as $\bar{X} = [X, Y, Z, \dot{X}, \dot{Y}, \dot{Z}]^T = [\bar{R}_{N,sc}, \bar{V}_{N,sc}]^T$. The equations of motion governing the spacecraft, assumed to possess a comparatively negligible mass, are then written as

$$\ddot{\bar{R}}_{N,sc} = -GM_N \left(\frac{\bar{R}_{N,sc}}{R^3_{N,sc}} \right) + G \sum_{i=1}^{N_b} M_i \left(\frac{\bar{R}_{sc,i}}{R^3_{sc,i}} - \frac{\bar{R}_{N,i}}{R^3_{N,i}} \right) \tag{4}$$

where the subscripts N and sc indicate Neptune and the spacecraft, M_i is the mass of body i, G is the universal gravitational constant, $\dot{(.)}$ indicates a time derivative with respect to an observer in the inertial frame, and $\bar{R}_{i,j}$ indicates the position vector measured from body i to body j. The DE440 lunar and planetary ephemerides, maintained by NASA's Navigation and Ancillary Information Facility (NAIF),[17,18] are used to locate each celestial body at each epoch during numerical integration.[19] Additionally, the naif0012 file is used for the accurate conversions between UTC and Ephemeris Time and the pck00011 kernel is used to obtain the axis orientation for the inertial frames. The SPICE kernels nep097, nep095 and nep102 are included to obtain the accurate position of Neptune's satellites. The solution space of this n-body problem is chaotic, but solutions from the Neptune-Triton CR3BP may be approximately retained in the point mass ephemeris model.

Numerically Correcting Trajectories

In this paper, two corrections schemes are used. First, coarsely-generated initial guesses are corrected and optimized in the Neptune-Triton CR3BP using collocation. Then, these transfers are corrected to produce a continuous path in the ephemeris model using multiple-shooting. These two different corrections schemes are selected based on the requirements of each correction step. In the first step, collocation is better suited to robustly generating continuous paths from discontinuous initial guesses at the expense of lower accuracy due to the representation of a curve as a sequence of polynomials. In the second step, multiple shooting is used to generate a path in the point mass ephemeris model of the Neptunian system using the solution that was previously corrected in the CR3BP. In this case, the initial guess lies close to the corrected transfer and the solution is more accurate as each arc is propagated in the dynamical system.

In this paper, the collocation scheme is implemented using the approach presented by Grebow and Pavlak[20] and previously used to correct primitive-based initial guesses by Smith and Bosanac.[11] In this implementation, the initial guesses are first split into m segments and each segment is then split into n arcs. Then, p collocation nodes are distributed along each arc. The number and location of the nodes are influenced by the type and order of collocation scheme. In this case, the collocation scheme is obtained through a 7-th order polynomial with a Legendre-Gauss-Lobatto (LGL) node spacing strategy. Therefore, $p = 7$ nodes are placed along each arc. The k-th node of the j-th arc within the i-th segment is described by the state vector $\boldsymbol{x}^i_{j,k}$ and the time elapsed from the first node along the entire trajectory is identified with $t^i_{j,k}$. The nodes are placed along each arc at normalized times that are equal to the roots of the derivative of the $(p-1)$-th order Legendre polynomial.[20–22] This normalized time is defined as $\tau = 2((t - t^i_{j,1})/\Delta t^i_j) - 1 \in [-1, 1]$ where Δt^i_j is the elapsed time from the beginning of the arc. The odd-numbered nodes, i.e. $k = 1, 3, 5, 7$ are defined as free nodes and are used to fit the polynomial along the arc, while the even-numbered nodes $k = 2, 4, 6$ are the defect nodes and are used to assess the differences between the polynomial representation and the value of the states computed with the system dynamics.

The trajectory is described using a free variable vector $\boldsymbol{V}_i$ that includes the state and time at the free nodes of each arc in the i-th segment. For the i-th segment, the free variable vector is computed as

$$\boldsymbol{V}_i = \left[\begin{bmatrix} \boldsymbol{x}^i_{1,1} \\ \boldsymbol{x}^i_{1,3} \\ \boldsymbol{x}^i_{1,5} \end{bmatrix}^T \quad \begin{bmatrix} \boldsymbol{x}^i_{2,1} \\ \boldsymbol{x}^i_{2,3} \\ \boldsymbol{x}^i_{2,5} \end{bmatrix}^T \quad \dots \quad \begin{bmatrix} \boldsymbol{x}^i_{n_i-1,1} \\ \boldsymbol{x}^i_{n_i-1,3} \\ \boldsymbol{x}^i_{n_i-1,5} \end{bmatrix}^T \quad \dots \quad \begin{bmatrix} \boldsymbol{x}^i_{n_i,1} \\ \boldsymbol{x}^i_{n_i,3} \\ \boldsymbol{x}^i_{n_i,5} \\ \boldsymbol{x}^i_{n_i,7} \end{bmatrix}^T \quad \begin{bmatrix} \Delta t^i_{1,i} \\ \Delta t^i_{2,i} \\ \vdots \\ \Delta t^i_{n_i,i} \end{bmatrix}^T \right] \tag{5}$$

and the trajectory free variable vector $\boldsymbol{V}$ is formed by the free variable vectors $\boldsymbol{V}_i$ for all m segments, resulting in a total of $((3p-2)\sum_{i=1}^m n_i + 6m)$ variables. Note that the last node of the j-th arc overlaps with the first node of the subsequent arc. Accordingly, the node $\boldsymbol{x}^i_{j,7}$ is not included in $\boldsymbol{V}_i$.

To capture the constraints that a continuous trajectory must satisfy, a constraint vector $\boldsymbol{F}(\boldsymbol{V})$ is defined. A constraint vector $\boldsymbol{F}_c$ enforces continuity between subsequent segments and is equal to

$$\boldsymbol{F}^i_c = \begin{cases} (\boldsymbol{x}^{i+1}_{1,1} - \boldsymbol{x}^i_{n_i,p})^T \text{ if natural motion} \\ (\boldsymbol{r}^{i+1}_{1,1} - \boldsymbol{r}^i_{n_i,n})^T \text{ if impulsive maneuver applied} \end{cases} \tag{6}$$

for $i < m$. The constraint vector $\boldsymbol{F}_d$ constrains the polynomial representation of each arc to accurately describe the dynamics at the defect nodes along each arc. This constraint along the j-th arc of the i-th segment is computed as

$$\boldsymbol{F}^i_{d,j} = \begin{bmatrix} (\dot{\boldsymbol{q}}^i_{j,2}(\tau_2) - \dot{\boldsymbol{x}}^i_{j,2})w_2 \\ (\dot{\boldsymbol{q}}^i_{j,4}(\tau_4) - \dot{\boldsymbol{x}}^i_{j,4})w_4 \\ (\dot{\boldsymbol{q}}^i_{j,6}(\tau_6) - \dot{\boldsymbol{x}}^i_{j,6})w_6 \end{bmatrix}^T \tag{7}$$

where w_k is the LGL weight associated with the k-th collocation node, $\dot{\boldsymbol{q}}$ is the derivative of the polynomial along the arc with respect to normalized time τ, and $\dot{\boldsymbol{x}}$ is the normalized time derivative of the state vector $\boldsymbol{x}^i_{j,k}$ calculated as

$$\dot{\boldsymbol{x}}^i_{j,k} = \frac{\Delta t^i_j}{2} \boldsymbol{g}(\boldsymbol{x}^i_{j,k}) \tag{8}$$

where $\boldsymbol{g} = [\dot{x}, \dot{y}, \dot{z}, \ddot{x}, \ddot{y}, \ddot{z}]$. For all n_i arcs along the i-th segment, the defect constraint vector is

$$\boldsymbol{F}^i_d = \left[\boldsymbol{F}^i_{d,1}, \boldsymbol{F}^i_{d,2}, \dots, \boldsymbol{F}^i_{d,n_i}\right] \tag{9}$$

Therefore, the constraint vector $\boldsymbol{F}(\boldsymbol{V})$ imposed on the entire trajectory is

$$\boldsymbol{F}(\boldsymbol{V}) = \left[\boldsymbol{F}^1_c, \boldsymbol{F}^2_c, \dots, \boldsymbol{F}^{m-1}_c, \boldsymbol{F}^1_d, \boldsymbol{F}^2_d, \dots, \boldsymbol{F}^m_d\right]^T \tag{10}$$

This constraint vector is used to update the free variable vector $\boldsymbol{V}$ using Newton's method until the norm of the constraint vector is equal to zero to within a tolerance of 10^{-12}.

In this paper, the collocation scheme includes a mesh refinement method, which redistributes arcs and nodes along the segments to improve the polynomial approximation of the trajectory. For a trajectory composed of m segments and n_i arcs along the i-th segment, the placement of the collocation nodes is mathematically defined, regardless of the characteristics of the trajectory. However, nodes will be placed further apart along long trajectories and very close to each along smaller trajectories. As a consequence, the polynomial fitting of the free nodes might result in a more or less accurate representation of each arc compared to the true solution of the dynamical system. This difference causes some arcs to have a higher error at the defect nodes. Accordingly, mesh refinement is used to equally distribute the error on the defect nodes along the arcs of the solution.[23] In this paper, hybrid mesh refinement is implemented using the approach presented by Grebow and Pavlak and the method for error redistribution by Carl de Boor;[20,24,25] this approach was also used by Smith and Bosanac for primitive-based initial guesses correction.[11]

To describe a trajectory in the multiple-shooting corrections problem, the free variable vector is constructed using the states and the epoch of a sequence of nodes that are located along the continuous trajectory that exist in the CR3BP. In this paper, a selected number of nodes are sampled at equal intervals in the arclength along a continuous path, with nodes also placed at any location where an impulsive maneuver is allowed. The node placement discretizes the continuous trajectory in N arcs. Then, the state of each node is first transformed from the Neptune-Triton rotating frame into the Neptune-centered inertial frame and is labeled as $\mathbf{X}_i$. Similarly, the epoch t_i at the beginning of the i-th arc and its associated propagation time Δt_i are converted from nondimensional time to ephemeris time. All the states and times are nondimensionalized using the characteristic quantities of the Neptune-Triton CR3BP to facilitate numerical propagation.[26] Using these definitions, the free variable vector is defined as

$$\mathbf{V} = [\mathbf{x}_{1,t_0}, t_1, \Delta t_1, \mathbf{x}_{2,t_0}, t_2, \Delta t_2, ..., \mathbf{x}_{N,t_0}, t_N]^T \tag{11}$$

where the subscript t_0 represents the state at the beginning of the i-th arc, t_i is the initial epoch of the i-th arc and Δt_i is its propagation time.

To correct the maneuver-enabled trajectory to be continuous, a constraint vector is defined. The constraint vector is equal to

$$\begin{aligned}\mathbf{F} =& [\mathbf{x}_{1,t_f} - \mathbf{x}_{2,t_0}, t_2 - (t_1 + \Delta t_1), ..., \mathbf{s}_{m-1,t_f} - \mathbf{s}_{m,t_0}, t_m - (t_{m-1} + \Delta t_{m-1}), ..., \\ & \mathbf{x}_{n-1,t_f} - \mathbf{x}_{n,t_0}, t_n - (t_{n-1} + \Delta t_{n-1})]^T\end{aligned} \tag{12}$$

where the subscript t_f represents the state at the end of the i-th arc. If a maneuver occurs immediately before the state at epoch, then t_m and $\mathbf{s}_{m,i}$ represents the position vector at the beginning of the associated arc. The free variable vector is updated via Newton's method until the norm of this constraint vector equals zero to within 10^{-8}.

Constrained Local Optimization

Continuous transfers obtained in the Neptune-Triton CR3BP via collocation are optimized to balance reducing the maneuver magnitude with geometrically resembling the initial guess. This optimization is performed using constrained local optimization via `fmincon` with the *sqp* algorithm.[27,28] The free variable vector and the equality constraints vector used in these steps come from the collocation scheme described in the previous paragraph. In this paper, optimization is used to minimize a multi-objective cost function J which balances minimizing geometric differences between the current trajectory and initial guess with minimizing the total Δv. The objective function is mathematically defined as

$$J = w_{geo}(\Delta \boldsymbol{r}_{ig-ct})^2 + w_{man} \sum_{i=1}^{n_m} (\Delta v_i)^2 \tag{13}$$

where $\Delta \boldsymbol{r}_{ig-ct}$ is the difference between the position vectors of each collocation node along the initial guess and current trajectory, and Δv_i is the magnitude of the i-th of n_m impulsive maneuvers. The two competing objectives are balanced in J via two scalar weights, w_{geo} and w_{man}; these values are either set by the user or varied gradually in a continuation approach.

In addition to the equality constraints describing the collocation problem, additional path constraints are included. For an initial guess, the following inequality constraints can be used: maximum time of flight (TOF) as $TOF_{ig} \leq TOF_{max}$, maximum total Δv as $\Delta v_{TOT,ig} \leq \Delta v_{TOT,max}$, maximum or minimum single maneuver magnitude as $\Delta v_{i,min} \leq \Delta v_{i,ig} \leq \Delta v_{i,max}$, and the maximum or minimum distance from a body (Neptune P_1 or Triton P_2) as $d_{P_i,min} \leq d_{P_i,ig} \leq d_{P_i,max}$. These inequality constraints are appended to the constraint vector and additional rows added to the Jacobian matrix.

TECHNICAL APPROACH

An updated version of the motion primitive trajectory design, originally introduced by Smith and Bosanac,[11] is described in detail in this section. This approach consists of the following five steps:

1. Extract motion primitives that summarize the geometries of arcs along selected families of periodic orbits and their stable/unstable manifolds.
2. Generate a motion primitive graph, discretely approximating the potential connectivity of the motion primitives.
3. Search the motion primitive graph to produce one or more sequences of motion primitives that supply an initial guess for a trajectory.
4. Refine each initial guess to increase the likelihood of successful corrections.
5. Correct and optimize the initial guess to produce continuous trajectories with impulsive maneuvers in the CR3BP and then correct them in an ephemeris model.

Several steps of this process have been updated compared to the previous work from Smith and Bosanac as well as Miceli and Bosanac.[11,12] The primitive extraction process in Step 1 has been updated to produce higher quality clusters of geometrically similar arcs that are used to define motion primitives. In steps 2, 4 and 5, this paper demonstrates the capability to include path constraints in the graph and initial guesses construction and in the corrections processes. Step 3 has been modified to include a custom k-best search algorithm producing longer sequences of motion primitives that supply initial guesses with different geometries. Additionally, trajectories are now corrected in an ephemeris model to supply higher fidelity solutions in the final step of the primitive-based trajectory design process.

Step 1: Extract Motion Primitives

Motion primitives, which have been used in robotics, are described by Wolek and Woolsey as a set of fundamental building blocks of motion.[29] These primitives can be composed in a sequence to form more complex paths or actions. In this work, motion primitives are used to discretely summarize the geometries of arcs that lie along fundamental solutions that govern natural transport within the system; ongoing work is focused on extending these primitives to summarize more general arcs. These primitives are extracted using a clustering algorithm due to the complexity of categorizing nonlinear paths in a chaotic system where analytical expressions for geometry do not exist.

Motion primitives are used to summarize periodic orbits that exist in continuous families and arcs along segments of their global stable and unstable manifolds. In the case of hyperbolic invariant manifolds, arcs are sampled along the finite set of trajectories that are generated to discretely approximate a segment of the manifold. Each trajectory is first sampled at local maxima in the curvature, and split in windows of a user-defined n_{max} samples. The curvature along a nonlinear path is defined as[30]

$$\kappa(\boldsymbol{x}) = \frac{\sqrt{(\dot{x}\ddot{y} - \dot{y}\ddot{x})^2 + (\dot{z}\ddot{x} - \dot{x}\ddot{z})^2 + (\dot{y}\ddot{z} - \ddot{y}\dot{z})^2}}{(\dot{x} + \dot{y} + \dot{z})^{3/2}} \tag{14}$$

Unlike apses, time intervals, or arclength, this sampling approach adapts to the geometry of the arc, does not require specification of a reference point, is less sensitive to changes in speed along a trajectory, and does not require a priori knowledge of the solution characteristics. When $\dot{\kappa}(\boldsymbol{x}) = 0$ and $\ddot{\kappa}(\boldsymbol{x}) < 0$, a local maximum exists and seeds an initial condition for an arc. These initial conditions are propagated until the n_{max}-th next maximum in the curvature. These arcs form the dataset that is clustered and summarized to extract motion primitives for the stable or unstable manifold. For periodic orbits, no sampling is performed.

Each arc is a continuous path that must be discretely described prior to clustering and encoded in a finite-dimensional feature vector. This feature vector is calculated for each member of the dataset. Then, during the clustering process, the distance between two feature vectors captures the dissimilarity between two members. Thus, the feature vector must be formulated to capture the characteristics of interest in a specific application. In this paper, the goal is to capture geometric differences between two arcs. Accordingly, the feature vector for the i-th trajectory is defined using the position vectors at r states that are distributed evenly in the arclength. Mathematically, this vector is equal to

$$\boldsymbol{f}_i = \left[x_{i,1}, y_{i,1}, z_{i,1}, x_{i,2}, y_{i,2}, z_{i,2}, \ldots, x_{i,r}, y_{i,r}, z_{i,r}\right] \tag{15}$$

to produce a $3r$-dimensional vector. A set of arcs, either periodic orbits along a family or arcs along a stable or unstable manifold, are clustered by their geometry in a two-step process. This paper uses the Hierarchical Density-Based Spatial Clustering of Applications with Noise (HDBSCAN) algorithm.[31] This algorithm groups members of a dataset that exist in sufficiently dense regions of the feature vector space and are most stable across a hierarchy of all possible clusters. It is particularly well suited for identifying clusters of varying densities and effectively handles noise. Along with the feature vectors that describe each set of trajectories (i.e., one orbit family or arcs along one manifold), the hyperparameters $n_{min,core}$ and $n_{min,size}$ are also provided as an input to the algorithm. The smaller (or larger) these governing parameters are, the more localized (or global) variations they capture. HDBSCAN then outputs a set of labels, assigning each trajectory to a unique cluster or as noise. Except for those that lie at the border of a cluster, most of the noise points correspond to elements in less dense regions of the dataset that cannot be grouped with at least $n_{min,size} - 1$ other members. Those noise points are then input to HDBSCAN again for more localized clustering with smaller values of $n_{min,core}$ and $n_{min,size}$. Any smaller clusters generated in this localized clustering step are then appended to the set of clusters generated in the first step, adding distinct geometries but smaller groupings.

A motion primitive p is extracted to summarize cluster along with a small set of representative members. Specifically, the primitive is defined as the cluster medoid, i.e. the member of the cluster that is most similar to all other members. Additional members of each cluster are also stored to capture the region of the phase space, labeled roe, spanned by geometrically similar arcs, following the approach presented by Smith and Bosanac.[10] The primitives and additional members that summarize each cluster are stored in a library or database for use in the next step.

Step 2: Generate A Motion Primitive Graph with Constraints

The potential connectivity of motion primitives is represented using a graph structure. A graph is a set of nodes and edges that are used to model the relationships between objects existing in the same space.[32,33] Frazzoli as well as Majumdar and Tedrake have constructed motion primitive graphs by defining the nodes as motion primitives and using directed edges to connect primitives that may be sequentially composed to produce a nearby continuous path.[34,35] This graph discretely summarizes a continuous solution space.

Following the approach presented by Smith and Bosanac, a motion primitive graph is constructed in this work in two layers[10] At the lowest layer, the motion primitives belonging to a specific family of periodic orbits or hyperbolic invariant manifolds form the nodes of a subgraph. A user then specifies whether the primitives in this subgraph may be connected internally. If a subgraph is not internally connected, two or more motion primitives from that subgraph may not be sequentially composed. At the highest layer, each subgraph forms a node of an itinerary graph. The edges connecting the nodes of the itinerary graph are specified by the user, allowing them to impose any knowledge of the desired solution structure or lack thereof. These edges in the itinerary graph indicate whether primitives in two different subgraphs may be sequentially composed.

At both the subgraph and itinerary graph levels, each motion primitive may be connected to its k-nearest neighbors via a directed edge that is weighted by their potential for sequential composability. First, each primitive is sampled at s states, evenly distributed in the arclength. Then, $q_{i,j}$, the potential for primitive i and primitive j to be sequentially composed is calculated as

$$q_{i,j} = \min_{l \in [1,s]} \Big(\min_{m \in [1,s]} \big(\Delta r_{i_l, j_m} + (1 - \Delta\alpha(\vec{v}_{i_l, j_m})) \big) \Big) \tag{16}$$

where $\Delta r_{i_l,j_m}$ and $\Delta\alpha(\vec{v}_{i_l,j_m})$ are the differences in position and velocity direction between the l-th state on the i-th primitive and the m-th state on the j-th primitive. Accordingly, the sequential composability of two primitives captures a weighted sum of position and velocity discontinuities at the two nearest state vectors. When connections are allowed, a directed edge is added to the graph from one primitive to its k-nearest neighbors with the lowest values of the sequential composability.

In this paper, the graph construction step is enhanced to incorporate path and maneuver constraints. In this way, the graph can be modified to include only motion primitives or connections that satisfy the desired constraints. As a result, the complexity of the graph may be reduced and primitive-based initial guesses that are generated from this graph have a higher likelihood of satisfying the constraints. In this proof of concept, these constraints can include minimum or maximum periapsis or apoapsis distance from a primary and minimum or maximum magnitude of a Δv. The path constraints are implemented in the node generation step. If a motion primitive p_i or any of the trajectories in its roe_i violates a path constraint, those are removed from the primitive phase space set. A new motion primitive is identified from any trajectories in the roe_i that satisfy the constraints. Otherwise, if all the trajectories violate the constraint then the node representing that primitive is not included in the graph. Alternatively, the constraint on the magnitude of a single Δv is applied to the edges. When computing the edge weights between two primitives $q_{i,j}$, the velocity difference between the closest states is evaluated. If the magnitude of this velocity difference violates the constraint imposed on the Δv, then the edge is removed from the graph.

Due to the discrete nature of the motion primitive graph, the constraints imposed at the graph construction level should include a margin. For example, if the minimum closest passage to a primary is 300 km, the constraint applied to the graph could use a minimum periapsis altitude of 200 km. This margin can avoid excessive reduction of the solution space in the initial guess computation step. Then, the initial guesses that meet the constraints with a margin can be corrected using the actual constraints.

Step 3: Search the Motion Primitive Graph For Initial Guesses

The graph is searched to generate distinct primitive sequences that connect an initial arc to a final arc; these sequences form a coarse initial guess for a trajectory. This paper uses a modified k-best path search algorithm with A* to obtain k distinct paths through the graph. As a result, long sequences of primitives can be recovered in a computationally tractable manner.

To address the computation time and path similarity challenges of well-known k-best path algorithms, a variation of Yen's algorithm that uses A* is employed. The original version of A* was first proposed by Hart, Nilsson and Raphael[36] in 1968, to prove that a heuristic function could be incorporated into the formal mathematical theory of graph searching and achieve optimality when compared to other search algorithms. A* explores the neighboring nodes by computing a cost $c(n) = g(n) + h(n)$, which is the sum of the cost to go from the current node to the next, $g(n)$, and the cheapest expected cost to go from the next node to the target node, $h(n)$. All the incomplete paths and their relative cost up to the current node $c(n)$ are stored in a queue. When the exploration of the closest neighbors of the current node is complete, the algorithm orders the list of current incomplete paths in the queue, so that the node selected for the successive explorative iteration is the one that minimizes the total expected cost of the path. After reaching the target node, the search is concluded. The selection of the heuristic depends on the application of the graph. However, given a heuristic such that $h(n) \leq h^*(n)$, A* always returns the least expensive path from the start to the goal node, where $h^*(n)$ is the true or optimal cost to go from the current node to the goal node.[36] In this paper, $h(n)$ is the true best cost to go from the current node to the goal node, so $h(n) = min\sum_{i,j=1}^{T} q_{ij}$, where T is the number of all the primitives p_j connected with an edge to the primitive p_i. However, in some cases, the heuristic is computed as the minimum difference in Jacobi constant from the current node to the target node, $h(n) = min\sum_{i,j=1}^{T} \Delta C_{J,ij}$ to guide the search through the sequence of primitives with the smallest difference in C_J.

The k-best path algorithm presented in this paper is used to rapidly obtain k geometrically different sequences of primitives. The graph is first searched with A* to find the overall best path. After this is found, the edges composing the path are removed from the graph except for the last and/or first one; and the queue with the incomplete path is emptied. After completing these steps, A* explores the modified graph to search for a new path from the initial to the target node. The process is repeated until the list of best paths contains k elements. The described modifications are justified by some observations. First, to obtain k paths, removing the best path from the queue once it is found is necessary to enable iteratively searching the graph for additional paths. In addition, for a large and fully interconnected graph, the list of paths in the queue following the first best solutions are often subpaths or slight variations of the saved best path. If a node can reach any other node in the graph, the most optimal solution from that node is to always re-converge to the minimum cost path. Therefore, the subpaths created before arriving at the best path are removed from the queue and the connections between the nodes of the saved paths are removed from the graph, to avoid repetition of the same node sequences during the path search. The last and or first edges are not removed to prevent the complete disconnection of the starting node from the rest of the graph. Similar to how Yen's algorithm modifies the graph to ensure geometric diversity, this concept is taken to an extreme level here due to the edge density of a fully interconnected graph. Using this k-best path algorithm accelerates the process of searching for solutions through a large graph while guaranteeing solutions with enough geometric difference.

Step 4: Refine Initial Guesses

Once the k-best initial guesses are found, they are refined to obtain smoother sequences of motion primitive that minimize the state discontinuity. This refinement involves a morphing and a trimming step presented by Smith and Bosanac.[11] In the morphing step, two consecutive primitives of an initial guess and their regions of existence are considered at the same time. The morphing is obtained by analyzing the composability between the trajectories in the region of existence of the primitives and taking the pair that minimizes the discontinuity in position and velocity direction. For example, taking two primitive p_i and p_j, and their regions of existence roe_i and roe_j, the value $q_{i,j}$ is computed for every $r_i \in roe_i$ and $r_j \in roe_j$: two members of roe_i and roe_j that result in the lowest value of $q_{i,j}$ are used as part of the initial guess. After morphing, the selected initial guesses are trimmed at the sample states that minimize the value of $q_{i,j}$.

In this paper, the morphing and trimming steps are modified when a constraint has been applied to the graph generation step. In particular, this step is different only when the magnitude of a single Δv is constrained because the path constraints are already applied to the primitives and their associated representative members. When considering the constraint on a single maneuver, both the morphing and trimming steps are limited to pairs of primitives where the minimum value for $q_{i,j}$ is computed at a set of states x, y where $\Delta v_{x,y} \leq \Delta v_{max}$ and or $\Delta v_{x,y} \geq \Delta v_{min}$.

Step 5: Correct And Optimize Initial Guesses With Constraints

The initial guesses are corrected and optimized in the Neptune-Triton CR3BP via collocation and then corrected in the ephemeris model via multiple shooting. For each initial guess, the initial mesh parameters for the collocation correction are specified by the user, and the maneuver locations can be placed at any of the nodes of the mesh and at the initial or final state of each primitive. For example, if some of the mesh nodes are placed at apsis along the primitives, then maneuvers can be placed at those states.

Using the collocation-based optimization scheme, the weights of the objective function are gradually modified to recover a maneuver-optimal solution in the Neptune-Triton CR3BP. First, the initial guess is used to recover a nearby continuous solution with $w_{geo} = 1$ and $w_{man} = 0$, prioritizing resembling the initial guess. Once corrected, the transfer is optimized in a continuation scheme using the same optimization algorithm, but varying the weights from $w_{geo} = 1$ and $w_{man} = 0$ to $w_{geo} = 0$ and $w_{man} = 1$ in a user-defined number of steps s. As a result of this process, the transfers at each step gradually evolve away from the initial guess as the total maneuver magnitude decreases. If desired, path and/or maneuver constraints may be added during the correction and optimization step. Unlike the graph construction step, these constraints do not incorporate any margin in their values.

Finally, the optimal transfers in the CR3BP are corrected in the ephemeris model using multiple shooting. In this implementation, the central body is Neptune and the secondary bodies are the Neptunian moons: Triton, Naiad, Thalassa, Despina, Galatea, Larissa, Hippocamp, Proteus, Nereid, Halimede, Sao, Laomedeia, Psamathe, Neso. Although these trajectories are corrected in the inertial frame, they may also be analyzed in the Neptune-Triton rotating frame.

RESULTS

The updated motion primitive process presented in this paper is used to compute a set of trajectories that exist within the trajectory tradespace for a Neptune mission, focused on the phase that begins from the interplanetary arrival into the Neptunian system and ends with insertion into a science orbit. The analysis presented in this paragraph considers two arrival conditions and two potential target orbits. For each target orbit, a graph is user-constructed by selecting the most appropriate set of motion primitives. The graphs are searched to obtain the k-best and geometrically distinct initial guesses, that are then corrected and optimized. The TOF and total Δv of these trajectories are used to capture part of the trajectory trade space. In this paper, this process is applied to transfers that are computed with and without constraints to compare the results.

Graph Construction

The two initial conditions used in this paper are selected as periapses with respect to Neptune along two different interplanetary transfers. These two states, labeled as Neptune Orbit Insertion (NOI) states, are described in Table 1. These states have been propagated backwards and forward in time respectively for 3.5 days in the rotating frame to obtain the trajectory arcs represented in red in Figure 1. The original initial conditions have out-of-plane components with respect to the Neptune-Triton plane. However, a planar version of these trajectories is used for the demonstrative purpose of this study and the spatial case will be the subject of future analysis. The planar orbit insertion arcs are plotted in blue in Figure 1. These two initial arcs are for the first set of nodes that are included in the motion primitive graph.

Table 1. Neptune Orbit Insertion Characteristics

Property	NOI State 1	NOI State 2
Epoch at apsis	October 2, 2045, 11:52:51 UTC	January 11, 2052, 14:22:33 UTC
Periapsis altitude	2460.11 km	1300.00 km
Hyperbolic excess velocity	v_∞: 11.5252 km/s	v_∞: 8.83 km/s
Declination angle	$\delta = 8.3778°$	$\delta = 9.3076°$
Jacobi Constant	$C_J = 0.950385$	$C_J = 0.896031$

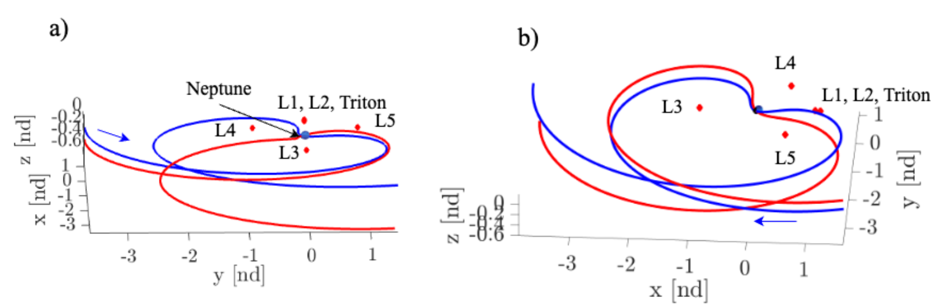

Figure 1. View of the spatial (red) and planar (blue) arcs leading to the first orbit insertion point (a) and the orbit second insertion point (b).

Two different resonant orbits have been selected as the target of the transfer and supply the final node of each graph. The first target is a $3 : 4$ resonant orbit with a Jacobi constant of $C_J = 1.75598$. This orbit allows for two Triton's flybys at altitudes lower than 300 km and at two different locations along its orbit around Neptune. The mission orbit is selected to support measuring the magnetic induction at Triton when crossing Neptune's magnetic field, as discussed in Cochrane et al.[37] Such science would support the identification of potential subsurface oceans on Triton, confirming its ocean world classification; which represents a fundamental goal of a future mission to the Neptune system. The second target orbit has been selected to be a $1:4$ resonant orbit with periapsis with respect to Neptune outside of Neptune's rings, to allow for an in situ measurement of their composition. The characteristics of both target orbits are listed in Table 2 and are plotted in the rotating frame in Figure 2. The selected orbits represent the final node of two different graphs.

Table 2. Target Orbits Characteristics

Property	3:4 Resonant Orbit	1:4 Resonant Orbit
Period	23.2441 days	23.5059 days
Periapis to Neptune	$34,247.993$ km	$135,761.897$ km
Periapis to Triton	$1,353.753$ km	$218,998.103$ km
Semi-major axis	$477,362.857$ km	$893,931.923$ km
Jacobi Constant	$C_J = 1.75598$	$C_J = 2.07803$

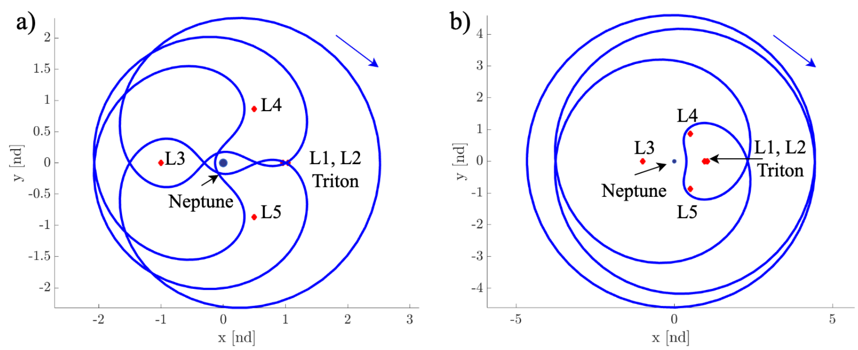

Figure 2. Target orbits in the Neptune-Triton CR3BP: a) 3:4 resonant orbit and b) 1:4 resonant orbit.

Once the initial and final nodes of each graph are selected, the remaining part of the graph can be generated by adding motion primitive sets, selected to have similar Jacobi constant values and geometries to the initial and final orbits of the transfer. For this paper, the two graphs are composed of two different sets of motion primitives, which include the following periodic orbits: L_3 Lyapunov orbit family; distant retrograde orbit family; 1:2, 1:3, 1:4, 1:5, and 3:4 prograde resonant orbit families with periapsis on the $-\hat{x}$-axis; 1:2, 1:3, and 1:4 prograde resonant orbit families with periapsis on the $\hat{x}$-axis; 2:3, 3:5 and 4:5 prograde resonant orbit families; 3:1 retrograde resonant orbit families with periapsis on each of the $+\hat{x}$- and $-\hat{x}$-axes; and 4:1 retrograde resonant orbit family. Motion primitives summarizing stable and unstable manifolds of the following orbits also included: 7 members of the 1:2 prograde resonant orbit family with $C_J = [1.50, 1.56, 1.61, 1.65, 1.70, 1.75, 1.81]$; 6 members of the 1:3 prograde resonant orbit family with $C_J = [1.22, 1.30, 1.35, 1.40, 1.45, 1.51]$; 4 members of the 1:4 prograde resonant orbit family with $C_J = [1.15, 1.17, 1.20, 1.25]$; 5 members of the 1:5 prograde resonant orbit family with $C_J = [1.09, 1.10, 1.12, 1.13, 1.15]$. For these manifolds, given that the in-plane instability of the resonant orbits used to generate the manifolds is close to 2, only the trajectory arcs that sufficiently depart the orbits have been stored and used in the motion primitive generation step. Finally, the graph includes primitives extracted from the stable manifolds of the 3:4 resonant target orbit.

The motion primitives have been extracted as detailed in Step 1 of the Technical Approach Section. In particular, the manifolds have been first split in smaller arcs defined by an even number of maxima in curvature, e.g. one arc along a $1 : 2$ resonant orbit manifold includes 2 maxima in curvature, and then sampled in 25 nodes equally spaced in arclength. On the other side, the motion primitives for the periodic orbits are obtained by considering the whole orbits and sampling them in the maxima in curvature as presented by Miceli, Bosanac, Stuart and Alibay.[12] In both cases, the feature vectors contain the position components at the sample nodes. An example of the motion primitives extracted from a periodic orbit family and an invariant manifold is provided in Figure 3.

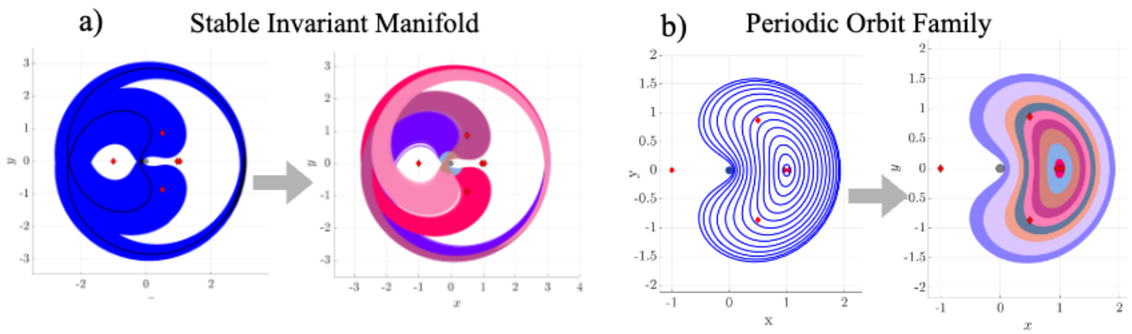

Figure 3. a) Set of clusters obtained from a stable invariant manifold of seven 1:2 resonant orbits with initial conditions on $-X$-axis. b) The clusters obtained from the distant retrograde orbit family.

The motion primitives in the two graphs are interconnected between the initial and final nodes as presented in the high-level itinerary graph Figure 4 and Figure 5. The primitives within the transfer set are all connected bidirectionally, i.e. one primitive can be reached from any other primitive in the set. Additionally, each of the primitives belonging to the same families are internally connected. These properties are represented by the symbols at the top right corner of the transfer set box and on the top right corner of each family icon.

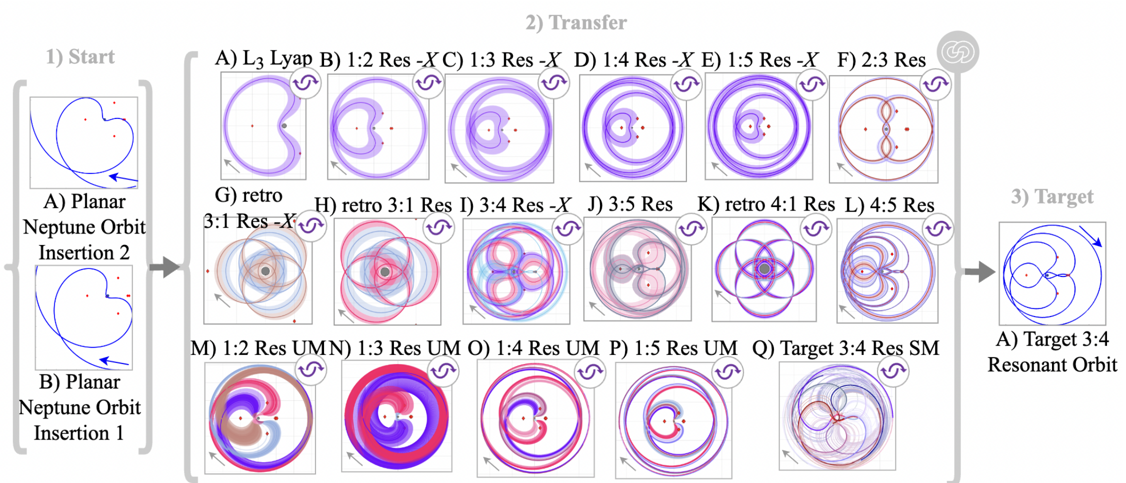

Figure 4. High-level itinerary graph showing the connection between the motion primitives selected to reach the 3:4 resonant orbit. Purple arrows indicate that the primitives within the family are internally connected. The gray arrow indicates that all the motion primitive families are connected with bidirectional edges.

Both graphs are generated first without any constraints and then adding two different constraints. Specifically, a minimum periapsis distance from Neptune of $30,000$ km is added to the graph targeting the 3:4 resonant orbit, and a maximum single Δv of 2.0 km/s is added to the graph targeting the 1:4 resonant orbit.

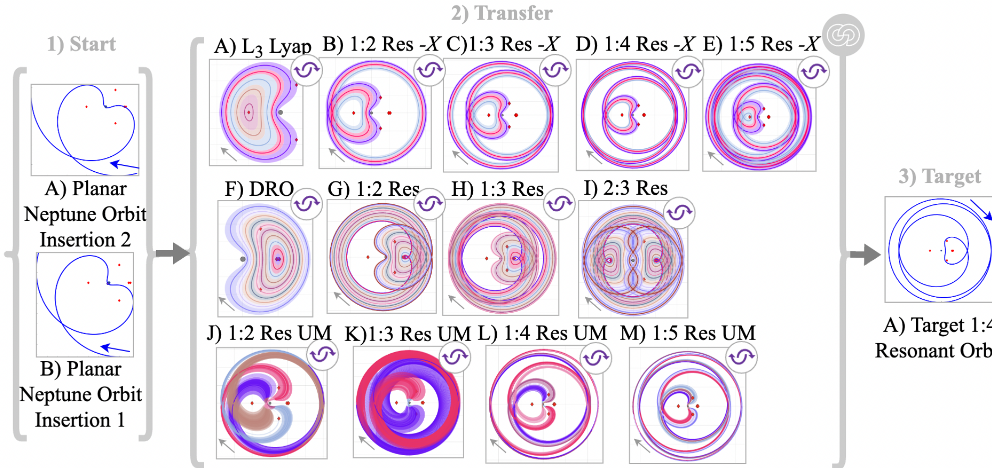

Figure 5. High-level itinerary graph showing the connection between the motion primitives selected to reach the 1:4 resonant orbit. Purple arrows indicate that the primitives within the family are internally connected. The gray arrow indicates that all the motion primitive families are connected with bidirectional edges.

In the first case, the goal is to obtain a transfer that does not intersect with the ring region around Neptune, which ranges from $40,000$ km to $57,000$ km. Imposing a lower periapsis constraint in the graph construction phase helps filter the solution space while considering some margin on the constraints. Similarly, in the second case, the maximum single maneuver magnitude constraint has been considered with a higher value compared to the desired constraint to allow some flexibility in the graph construction. This constraint aims to target transfers from the NOI that perform various smaller maneuvers to get to a low energy level, rather than allowing them to reach the same orbit with fewer but more expensive maneuvers.

Initial Guesses

The initial guesses resulting from the constrained and unconstrained graph are compared. Selected geometrically different initial guesses generated by searching the graph in Figure 4 are shown in the first and third rows of Figure 6 and Figure 7; both cases target a 3:4 resonant orbit in the Neptune-Triton system but start from a different orbit insertion. In the figures, the first row of initial guesses is obtained by searching the unconstrained graph and the third row displays initial guesses from the constrained graph. From the comparison of the solutions between the constrained and unconstrained graph, it is visible how the addition of the constraint of min distance from Neptune $\min(h_{P1} > 30.000)$ over the graph produces initial guesses with primitives existing further away from the first primary and connecting to different parts of the initial and final arcs to fulfill the minimum distance requirement. Similarly, the initial guesses in the first and third rows of Figure 9 and Figure 10 are affected by the application of the single $\Delta v < 2$ km/s constraints over the graph in Figure 5. The introduction of this constraint is not particularly visible from the initial guesses in this case since the constraint acts on the maneuver cost. However, the edges and nodes for both graphs are considerably reduced when introducing respectively the limit on the single maneuver or the minimum distance from a body. For this reason, the constraints on this step are always considered with a margin, as mentioned in the previous paragraphs. Overall, all the initial guesses show a smooth transition between pairs of motion primitives due to the minimization of the edge weight value $q_{i,j}$, which captures the variation of the velocity direction in addition to the discontinuity in position.

Final Transfers and Trade Space

The initial guesses are corrected placing maneuvers between discontinuous primitives and at periapsis with Neptune and imposing the associated constraints. For this case study, a minimum distance from Neptune of

57.000 km is imposed on the transfers targeting the 3:4 resonant orbit, whereas a max single Δv of 1.8 km/s is applied to the transfers targeting the 1:4 resonant orbit. With the first constraint, we impose that transfer to reach the target orbit is performed outside of the main ring region around Neptune, which terminates at a radius of 63.000 km from the planet's center. In the second case, we force the trajectories to perform the energy change from the orbit insertions to the target trajectory in smaller maneuvers and avoid more expensive and shorter transfers. The final trajectories for both scenarios are visible in the second and fourth rows of Figures 6, 7 and Figures 9, 10, where the grey arcs are the initial and final state of the transfer and the red circles identify maneuvers locations.

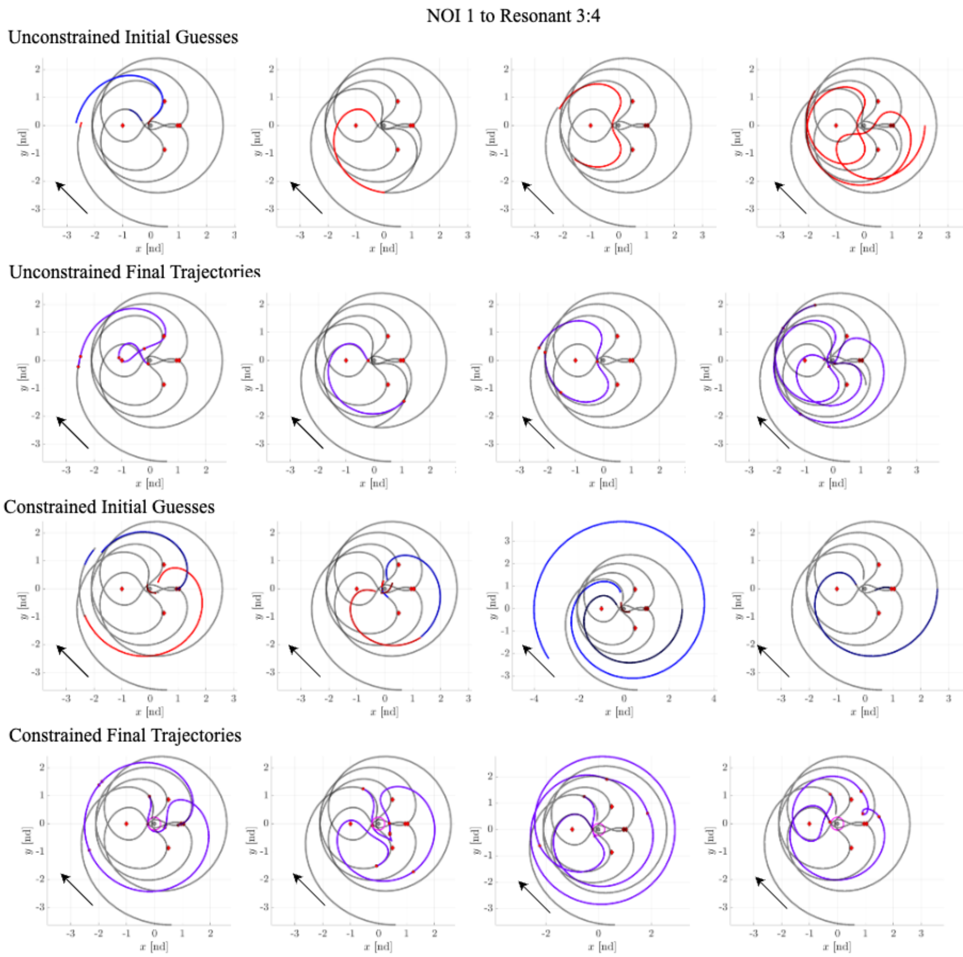

Figure 6. A sample of four transfers generated from the graph in Figure 4 to go from the first NOI arc to a 3:4 resonant orbit. On the first two rows, the initial guesses and the final transfers obtained from the unconstrained graph. On the third and fourth rows, the initial guesses and the final transfers obtained from the constrained graph. The final altitude constraint of 57.000 **km altitude is indicated with the pink circle.**

For the transfer to the 3:4 resonant orbit, the final unconstrained trajectories in the first and second row in Figure 6 and Figure 7 show that the final transfers perform close passages to Neptune, with the periapsis close to the planet surface. In the third and fourth rows, the constrained trajectories are optimized considering the minimum altitude of 57.000 km from the planet's surface, which is represented with a magenta circle around Neptune, and only passes outside of that minimum altitude. Both the constrained and unconstrained final trajectories are evaluated in terms of the total time of flight and total Δv in Figure 8, where the transfers from the unconstrained initial guesses and graph are colored in red while the constrained trajectories are colored in blue. Additionally, the solutions coming from the first orbit insertion are represented by a square, while the circle states the solutions obtained from the second orbit insertion arc. As expected, the unconstrained solutions, that can perform maneuvers at a closer distance to the first primary are generally characterized by lower total Δv, with the solutions starting from the second NOI being on average more expensive due to the higher difference in energy with the target orbit compared to the first orbit insertion. The constrained solution in this case also causes a longer TOF, especially for the transfers obtained from the first orbit insertion. Overall, only a few of the unconstrained solutions among the selected ones have a total Δv below 2 km/s which can be considered the maximum cost to perform orbit insertion and start a science phase for this mission scenario. No solution is below a 1.5 km/s total maneuver cost (dashed line), representing the best value for an orbit insertion maneuver in the Neptunian system. However, this study case is intended to demonstrate the applicability of different mission constraints on the motion primitive trajectory design approach and the presented results show only an example of the possible diverse geometries obtainable with this approach. It is possible that imposing additional constraints on the same graph could result in a set of transfers that meet the desired orbit insertion maneuver cost.

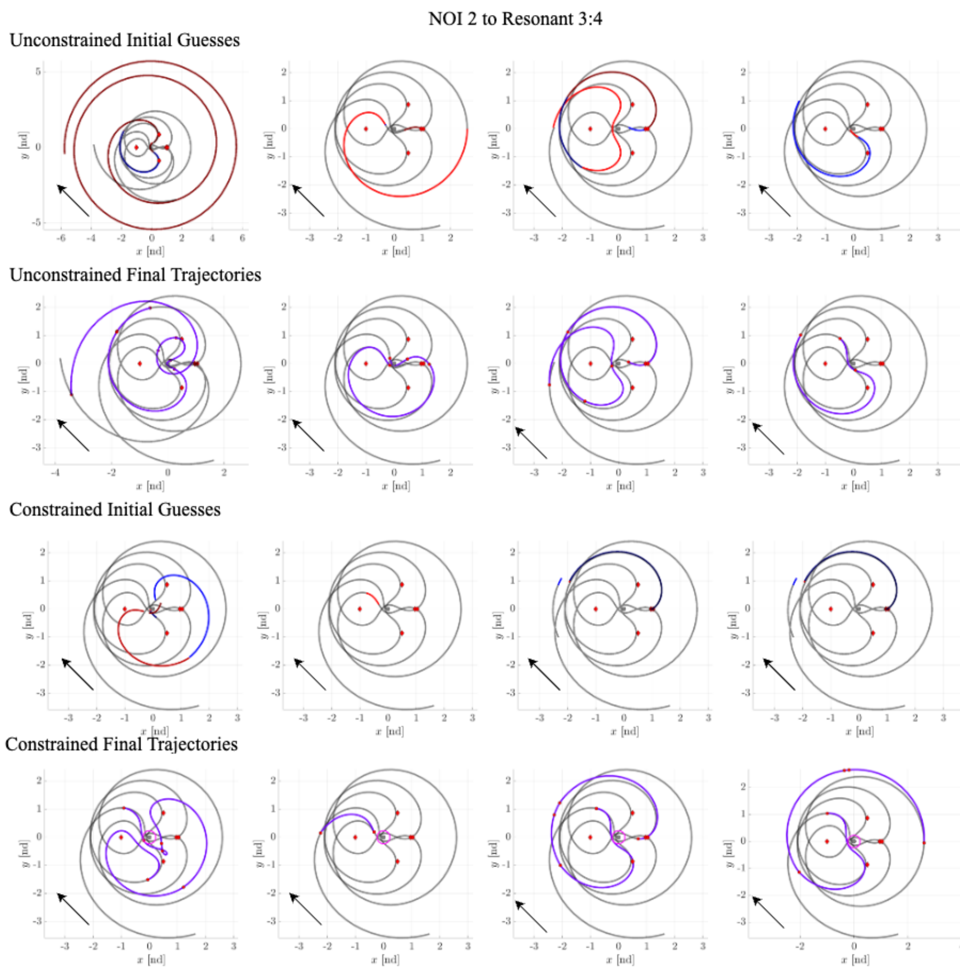

Figure 7. A sample of four transfers generated from the graph in Figure 4 to go from the second NOI arc to a 3:4 resonant orbit. On the first two rows, the initial guesses and the final transfers obtained from the unconstrained graph. On the third and fourth rows, the initial guesses and the final transfers obtained from the constrained graph. The final altitude constraint of 57.000 km altitude is indicated with the pink circle.

The final solutions itinerary targeting a 1:4 resonant orbit from the first and second orbit insertion are presented in Figure 9 and Figure 10, where the second row shows the unconstrained solutions and the fourth row the constrained solutions. The final TOF and total Δv for this case are plotted in Figure 11 where, similarly as before, the squares represent the solutions starting from NOI 1 and the circles the solutions starting with NOI 2. Then, the orange indicates all the unconstrained solutions, while the light blue is used for the solutions obtained by constraining the single maneuvers. The majority of the constrained solutions lie within the bottom part of the plots, with one exception, indicating that the objective of the constraint of minimizing big single maneuvers was obtained. Moreover several of those solutions have a total Δv below the ideal value of 1.5 km/s, making the ideal candidates for a mission scenario. The behavior of this small sample of solution also indicates the expected behavior of a Δv - TOF pareto front, where the longer transfers can achieve lower total Δvs and vice-versa.

On the right side of Figure 8 and Figure 11, one of the lowest cost solutions is corrected in ephemeris and visualized in an inertial 'J2000' frame centered on Neptune. The magenta arc is the incoming leg from the interplanetary trajectory, the blue arcs are the set of revolutions obtained to transfer to the target orbit, which is represented in gray, using the maneuvers indicated with the red dots. From the trajectory in Figure 8, it is possible to see where the spacecraft will perform the close flybys with Triton along its orbits, targeting the scientific goal of this scenario. Similarly, the trajectory in Figure 11 shows the orbit insertion to the desired resonant orbit which has a periapsis with respect to Neptune that passes just on the outside of the planet's rings, allowing to perform in situ measurement of these interesting formations. This transfer is obtained with a total $\Delta v = 1.1366$ km/s, where every single maneuver indicated in the plot has the following values $\Delta v_i = [0.4143, 0.0096, 0.1159, 0.1441, 0.4501, 0.0012, 0.0012]$ km/s, with $i = [1, 7]$.

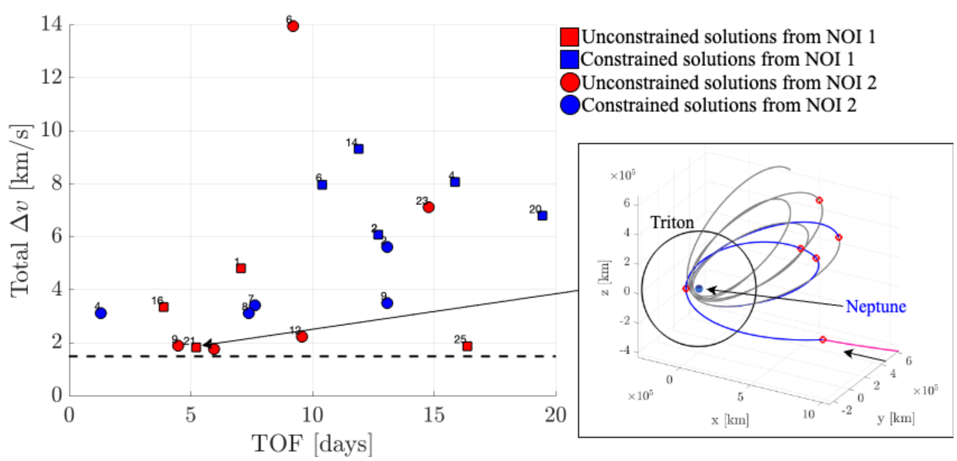

Figure 8. Trade space of solution for the transfer to a 3:4 resonant orbit. One of the best solutions corrected in ephemeris is shown in an inertial frame on the right.

CONCLUSIONS

This paper presents an updated version of the motion primitive trajectory design approach, first introduced by Smith and Bosanac[11] and then applied to a Neptune mission scenario by Miceli, Bosanac, Stuart and Albay.[12] The main novelty is the application of constraints to the transfers generated with the motion primitives, which consent to obtain trajectories with a specific distance from a primary, or total TOF, single maneuver cost, or total Δv. Additionally, updates have been added in the primitive extraction process to produce higher quality clusters of geometrically similar trajectory arcs, and in the initial guess search from the graph by introducing a custom k-best search algorithm. Finally, trajectories are now corrected in an ephemeris model to supply higher-fidelity solutions. This approach applied in the context of a Neptune mission targeting two different resonant orbits can produce a trade space of trajectories with a variety of geometries, that can meet any of the imposed constraints. For example, solutions that constrained the single maneuver cost resulted in trajectories with total Δv smaller than 1.5 km/s, ideal NOI cost, proving the feasibility of the motion primitives trajectory design technique.

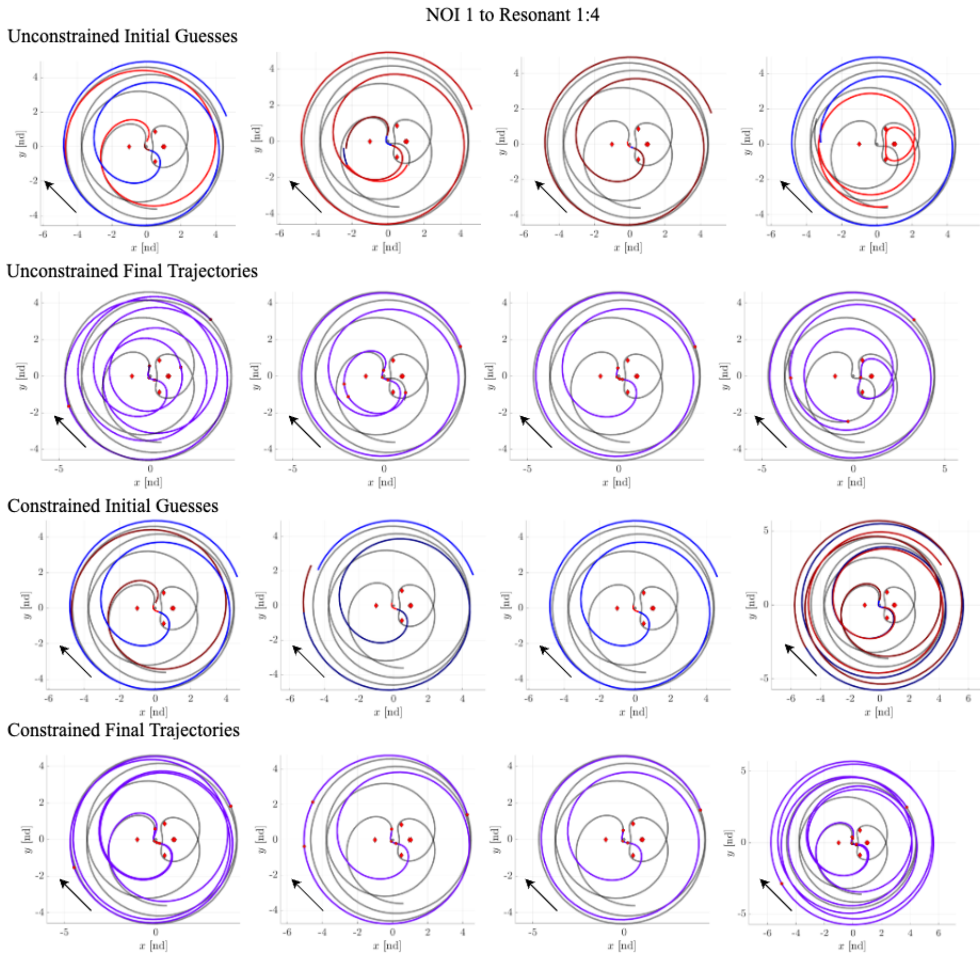

Figure 9. A sample of four transfers generated from the graph in Figure 5 to go from the first NOI arc to a 1:4 resonant orbit. On the first two rows, the initial guesses and the final transfers obtained from the unconstrained graph. On the third and fourth rows, the initial guesses and the final optimized transfers from the constrained graph.

ACKNOWLEDGMENTS

This work was completed at the University of Colorado Boulder with funding from the Strategic University Research Partnership program at the Jet Propulsion Laboratory, California Institute of Technology, under a contract with the National Aeronautics and Space Administration (80NM0018D0004). The authors would like to thank Dr. Jeffrey Stuart and Dr. Farah Alibay for their participation in the project that funded this work.

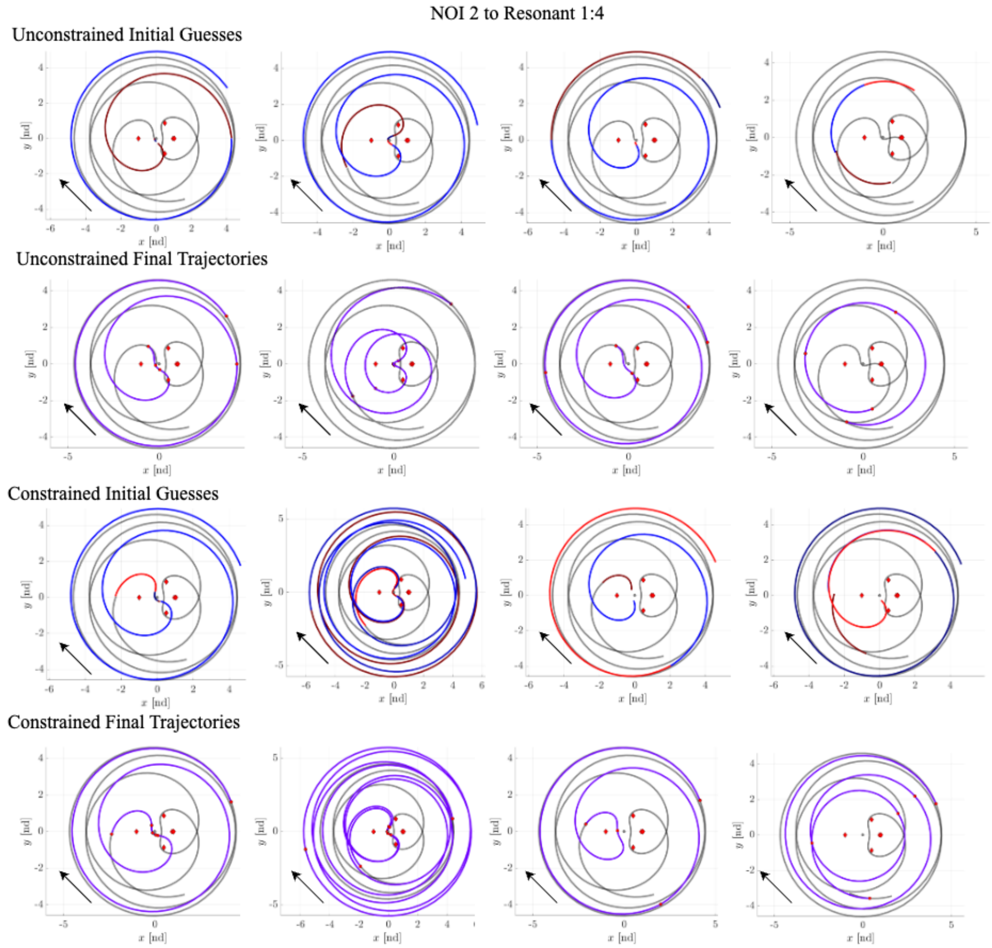

Figure 10. A sample of four transfers generated from the graph in Figure 5 to go from the second NOI arc to a 1:4 resonant orbit. On the first two rows, the initial guesses and the final transfers obtained from the unconstrained graph. On the third and fourth rows, the initial guesses and the final transfers from the constrained graph.

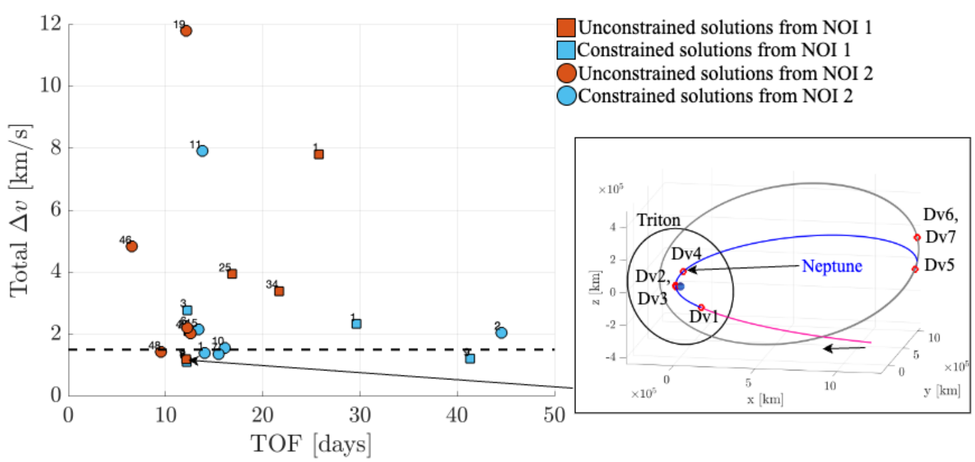

Figure 11. Trade space of solution for the transfer to a 1:4 resonant orbit. One of the best solutions corrected in ephemeris is shown in an inertial frame on the right.

REFERENCES

[1] National Academies of Sciences, Engineering, and Medicine, "NASA 2023 Decadal Survey," technical report, National Academies Press, Washington, D.C., 2023.

[2] R. Helled, N. Nettelmann, and T. Guillot, "Uranus and Neptune: Origin, Evolution and Internal Structure," *Space Science Reviews*, Vol. 216, No. 3, 2020, p. 38.

[3] B. Swenson, "Neptune atmospheric probe mission," *Guidance, Navigation and Control Conference*, American Institute of Aeronautics and Astronautics, 1992.

[4] A. Masters, N. Achilleos, C. Agnor, S. Campagnola, S. Charnoz, B. Christophe, A. Coates, L. Fletcher, G. Jones, L. Lamy, F. Marzari, N. Nettelmann, J. Ruiz, R. Ambrosi, N. Andre, A. Bhardwaj, J. Fortney, C. Hansen, R. Helled, G. Moragas-Klostermeyer, G. Orton, L. Ray, S. Reynaud, N. Sergis, R. Srama, and M. Volwerk, "Neptune and Triton: Essential pieces of the Solar System puzzle," *Planetary and Space Science*, Vol. 104, 2014, pp. 108–121.

[5] A. M. Rymer, K. D. Runyon, B. Clyde, J. I. Núñez, R. Nikoukar, K. M. Soderlund, K. Sayanagi, M. Hofstadter, L. C. Quick, S. A. Stern, T. Becker, M. Hedman, I. Cohen, F. Crary, J. J. Fortney, J. Vertesi, C. Hansen, I. d. Pater, C. Paty, T. Spilker, T. Stallard, G. B. Hospodarsky, H. T. Smith, H. Wakeford, S. E. Moran, A. Annex, P. Schenk, M. Ozimek, J. Arrieta, R. L. McNutt, A. Masters, A. A. Simon, S. Ensor, C. T. Apland, J. Bruzzi, D. A. Patthoff, C. Scott, C. Campo, C. Krupiarz, C. J. Cochrane, C. Gantz, D. Rodriguez, D. Gallagher, D. Hurley, D. Crowley, E. Abel, E. Provornikova, E. P. Turtle, G. Clark, J. Wilkes, J. Hunt, J. H. Roberts, J. Rehm, K. Murray, L. Wolfarth, L. N. Fletcher, L. Spilker, E. S. Martin, M. Parisi, M. Norkus, N. Izenberg, R. Stough, R. J. Vervack, K. Mandt, K. B. Stevenson, S. Kijewski, W. Cheng, J. D. Feldman, G. Allen, D. Prabhu, S. Dutta, C. Young, and J. Williams, "Neptune Odyssey: A Flagship Concept for the Exploration of the Neptune–Triton System," *Planet. Sci. J.*, Vol. 2, No. 5, 2021, p. 184.

[6] A. Simon, F. Nimmo, and R. C. Anderson, "Journey to an Ice Giant System: Uranus Orbiter and Probe," Planetary Mission Concept for the 2023–2032 Planetary Science Decadal Survey, June 7 2021. Retrieved May 1, 2022.

[7] S. Jarmak, E. Leonard, A. Akins, E. Dahl, D. Cremons, S. Cofield, A. Curtis, C. Dong, E. Dunham, B. Journaux, D. Murakami, W. Ng, M. Piquette, A. P. Girija, K. Rink, L. Schurmeier, N. Stein, N. Tallarida, M. Telus, L. Lowes, C. Budney, and K. Mitchell, "QUEST: A New Frontiers Uranus orbiter mission concept study," *Acta Astronautica*, Vol. 170, 2020, pp. 6–26.

[8] O. Mousis, D. Atkinson, T. Cavalié, L. Fletcher, M. Amato, S. Aslam, F. Ferri, J.-B. Renard, T. Spilker, E. Venkatapathy, P. Wurz, K. Aplin, A. Coustenis, M. Deleuil, M. Dobrijevic, T. Fouchet, T. Guillot, P. Hartogh, T. Hewagama, M. Hofstadter, V. Hue, R. Hueso, J.-P. Lebreton, E. Lellouch, J. Moses, G. Orton, J. Pearl, A. Sánchez-Lavega, A. Simon, O. Venot, J. Waite, R. Achterberg, S. Atreya, F. Billebaud, M. Blanc, F. Borget, B. Brugger, S. Charnoz, T. Chiavassa, V. Cottini, L. d'Hendecourt, G. Danger, T. Encrenaz, N. Gorius, L. Jorda, B. Marty, R. Moreno, A. Morse, C. Nixon, K. Reh, T. Ronnet, F.-X. Schmider, S. Sheridan, C. Sotin, P. Vernazza, and G. Villanueva, "Scientific rationale for Uranus and Neptune in situ explorations," *Planetary and Space Science*, Vol. 155, 2018, pp. 12–40. Surfaces, atmospheres and magnetospheres of the outer planets, their satellites and ring systems: Part XII.

[9] A. P. Girija, "A Flagship-class Uranus Orbiter and Probe mission concept using aerocapture," *Acta Astronautica*, Vol. 202, 2023, pp. 104–118.

[10] T. R. Smith and N. Bosanac, "Constructing Motion Primitive Sets to Summarize Periodic Orbit Families and Hyperbolic Invariant Manifolds in a Multi-Body System," *Celestial Mechanics and Dynamical Astronomy*, Vol. 134, No. 1, 2022, p. 7.

[11] T. R. Smith and N. Bosanac, "Motion Primitive Approach to Spacecraft Trajectory Design in a Multi-body System," *The Journal of the Astronautical Sciences*, Vol. 70, No. 34, 2023.

[12] G. E. Miceli, N. Bosanac, J. R. Stuart, and F. Alibay, *Motion Primitive Approach to Spacecraft Trajectory Design in the Neptune-Triton System*.

[13] V. Szebehely, *Theory of Orbits: The Restricted Problem of Three Bodies*. London: Academic Press, 1967.

[14] National Aeronautics and Space Administration (NASA), "Neptunian Satellite Fact Sheet," 2023. Accessed: 11-13-2023.

[15] NASA Navigation and Ancillary Information Facility (NAIF), "NASA Navigation and Ancillary Information Facility (NAIF) Generic Kernels," 2023.

[16] C. D. Murray and S. F. Dermott, *Solar system dynamics*. Cambridge university press, 1999.

[17] C. H. Acton, "Ancillary data services of NASA's Navigation and Ancillary Information Facility," *Planetary and Space Science*, Vol. 44, No. 1, 1996, pp. 65–70. Planetary data system.

[18] C. Acton, N. Bachman, B. Semenov, and E. Wright, "A look towards the future in the handling of space science mission geometry," *Planetary and Space Science*, Vol. 150, 2018, pp. 9–12. Enabling Open and Interoperable Access to Planetary Science and Heliophysics Databases and Tools.

[19] R. S. Park, W. M. Folkner, J. G. Williams, and D. H. Boggs, “The JPL Planetary and Lunar Ephemerides DE440 and DE441,” *The Astronomical Journal*, Vol. 161, feb 2021, p. 105.

[20] D. J. Grebow and T. A. Pavlak, “MCOLL: Monte Collocation Trajectory Design Tool,” AAS/AIAA Astrodynamics Specialist Conference, Stevenson, Washington, August 20-24, 2017, 2017.

[21] B. A. Conway, *Spacecraft Trajectory Optimization*. New York: Cambridge University Press, 2010.

[22] P. Williams, “Hermite-Legendre-Gauss-Lobatto Direct Transcription in Trajectory Optimization,” *Journal of Guidance, Control, and Dynamics*, Vol. 32, No. 4, 2009, pp. 1392–1395.

[23] R. E. Pritchett, *Strategies for Low-Thrust Transfer Design Based on Direct Collocation Techniques*. Thesis, Purdue University Graduate School, 2020.

[24] C. De Boor, “Good Approximation by Splines with Variable Knots. II,” *Proceedings of the Conference on the Numerical Solution of Differential Equations*, Dundee, Scotland, 1973.

[25] R. Russell and J. Christiansen, “Adaptive Mesh Selection Strategies for Solving Boundary Value Problems,” *SIAM Journal on Numerical Analysis*, Vol. 15, No. 1, 1978, pp. 59–80.

[26] D. Folta, N. Bosanac, I. Elliott, L. Mann, R. Mesarch, and J. Rosales, “Astrodynamics Convention and Modeling Reference for Lunar, Cislunar, and Libration Point Orbits,” tech. rep., NASA, 2022.

[27] MATLAB, *version R2006a*. Natick, Massachusetts: The MathWorks Inc., 2006-2009.

[28] J. Nocedal and S. J. Wright, *Numerical optimization*. Springer, 1999.

[29] A. Wolek and C. A. Woolsey, *Model-Based Path Planning*, pp. 183–206. Cham: Springer International Publishing, 2017.

[30] N. M. Patrikalakis, T. Maekawa, and W. Cho, *Shape Interrogation for Computer Aided Design and Manufacturing*. New York, NY: Springer, 2009.

[31] R. Campello, D. Moulavi, and J. Sander, “Density-Based Clustering Based on Hierarchical Density Estimates,” *Advances in Knowledge Discovery and Data Mining* (J. Pei, V. Tseng, L. Cao, H. Motoda, and G. Xu, eds.), Springer Berlin, Heidelberg, 2013, p. 160–172.

[32] J. Han, M. Kamber, and J. Pei, *Data Mining: Concepts and Techniques*. Waltham: Morgan Kaufmann Publishers, 2012.

[33] S. M. LaValle, *Planning Algorithms*. Cambridge: Cambridge University Press, 2006.

[34] E. Frazzoli, *Robust Hybrid Control for Autonomous Vehicle Motion Planning*. PhD Dissertation, Massachusetts Institute of Technology, Cambridge, MA, 2001.

[35] A. Majumdar and R. Tedrake, “Funnel Libraries for Real-Time Robust Feedback Motion Planning,” *Int. J. Robot. Res.*, Vol. 36, No. 8, 2017, pp. 947–982. DOI: https://doi.org/10.1177/0278364917712421.

[36] P. E. Hart, N. J. Nilsson, and B. Raphael, “A Formal Basis for the Heuristic Determination of Minimum Cost Paths,” *IEEE Transactions on Systems Science and Cybernetics*, Vol. 4, No. 2, 1968, pp. 100–107.

[37] C. J. Cochrane, R. R. Persinger, S. D. Vance, E. L. Midkiff, J. Castillo-Rogez, A. Luspay-Kuti, L. Liuzzo, C. Paty, K. L. Mitchell, and L. M. Prockter, “Single- and Multi-Pass Magnetometric Subsurface Ocean Detection and Characterization in Icy Worlds Using Principal Component Analysis (PCA): Application to Triton,” *Earth and Space Science*, Vol. 9, No. 2, 2022.